

# Electret MEMS Vibration Energy Harvester with Reconfigurable Frequency Response

Gen Hashiguchi<sup>1\*</sup> and Hiroshi Toshiyoshi<sup>2</sup>

<sup>1</sup>Department of Mechanical Engineering, Shizuoka University,  
3-5-1 Johoku, Naka-ku, Hamamatsu, Shizuoka 432-8011, Japan

<sup>2</sup>Institute of Industrial Science, The University of Tokyo,  
4-6-1 Komaba, Meguro-ku, Tokyo 153-8505, Japan

(Received March 1, 2023; accepted April 25, 2023)

**Keywords:** MEMS, vibrational energy harvester, electret, wide bandwidth, reconfigurable frequency response

We demonstrate a microelectromechanical systems (MEMS) electret-type vibrational energy harvester with a wide bandwidth between 25 and 60 Hz (span of 35 Hz) for a small sinusoidal acceleration of less than 10 mG ( $G = 9.8 \text{ m/s}^2$ ). We have developed a method of tailoring the nonlinear characteristics by adjusting the mutual position of the opposing electrodes. Both soft- and hard-spring effects are realized, thereby further extending the frequency bandwidth between 25 and 95 Hz so that power can be effectively retrieved from extremely small vibrations of 10 mG. This reconfigurable nature of the developed harvester device is suitable for autonomous distributed sensors that obtain power from environmental vibrations.

## 1. Introduction

Miniaturized vibrational energy harvesters have been developed as inexhaustible power sources for distributed sensor nodes. Studies have been performed to develop various harvesters using microelectromechanical systems (MEMS) technology.<sup>(1–11)</sup> Of particular interest is to realize a vibrational energy harvester with a wide frequency response in a low frequency range in order to enhance the efficiency of energy retrieval from environmental vibrations. For instance, our field work of the acceleration waveforms and its spectra measured on an actual viaduct of a highway<sup>(12)</sup> showed a distinguished vibration at 45 Hz and the power spectrum spreading between 10 and 200 Hz. Retrievable power is theoretically proportional to the integral of the power spectrum and the conversion efficiency over the frequency range. Therefore, a wide frequency response and a high conversion efficiency are required for vibrational energy harvesters.

Studies have been performed to develop vibrational power generation mechanisms in a wide frequency range. For instance, Liu *et al.* examined a piezoelectric cantilever-type vibrational energy harvester whose displacement was intentionally restricted by a mechanical stopper;<sup>(13)</sup>

---

\*Corresponding author: e-mail: [hashiguchi.gen@shizuoka.ac.jp](mailto:hashiguchi.gen@shizuoka.ac.jp)  
<https://doi.org/10.18494/SAM4367>

despite the linear mechanical motion, the spectrum peak of electrical output was flattened to effectively widen the bandwidth. This approach, however, would not work effectively under a low acceleration condition. Tang and Zuo employed a dual-mass vibration mechanism, which is a two-mass system linked with a spring damper.<sup>(14)</sup> They optimized the mechanical parameters of the two degree-of-freedom (DoF) mechanical systems and analytically showed a wide frequency response.<sup>(14)</sup> The use of a multiresonance mechanical structure reported by Masaki *et al.* is an approach similar to the use of a dual-mass system to realize wide-range vibrational energy harvesters.<sup>(15)</sup> Nguyen and Halvorsen reported an electrostatic energy-harvesting device using comb electrodes with double-clamped spring beams as an energy transducer.<sup>(16)</sup> They combined the electrostatic soft-spring nature of electrostatic force and the mechanical stress-hardening effect in the double-clamped beams, thereby widening the frequency response. However, the mechanical stroke was limited in the small gap of the comb electrodes, and thus the output power was limited to the 100 nW level.<sup>(16)</sup>

A bistable mechanism has also been investigated to realize a wide frequency range. The basic idea is to use the mechanical transition between two stable positions upon impulsive force application, which causes a damped oscillation at resonance. Impulsive force was generated by using two magnets attached to movable cantilevers, and energy harvesting was performed with a piezoelectric transducer.<sup>(17,18)</sup>

Ando and co-workers proposed a mechanical solution for a wide frequency range by using flexural pivots to support a proof mass, which moved between two stable states.<sup>(19,20)</sup> Cottone *et al.* also proposed a piezoelectric energy harvester made of mechanical buckling beams having bistability.<sup>(21)</sup>

As seen from the above-mentioned works and other studies, the bistability approach is effective for widening the frequency response. However, it inevitably comes with an activation energy barrier between two equilibrium points, which raises the threshold acceleration for transition, losing the adaptability to low-level environmental vibration. Therefore, the potential valley depth in the bistable mechanism should be carefully designed.

In this work, on the other hand, we used the bistability of an electrostatic kind for a different purpose, that is, the effective spring constant is lowered to adapt to weak environmental vibrations. A periodically modulated electrostatic potential has been newly created between the electrodes by using small arrays of protrusions attached to the electrode edges. The electrostatic attractive force acting between them has an effect of a virtual soft spring to lower the net spring constant of the entire system, thereby extending the bandwidth of the frequency response as well as making the harvester device adaptive to small environmental vibrations of a few mG ( $G = 9.8 \text{ m/s}^2$ ). The same structure has also been found to effectively harden the spring, depending on the initial condition of the mutual positioning of electrodes. In either case, the newly introduced electrode structures have the effect of extending the bandwidth.

For device implementation, we used a silicon-on-insulator (SOI) wafer with a 300-nm-thick active layer to form a MEMS vibrational energy harvester by deep reactive ion etching (DRIE). As a result, a wide bandwidth of 35 Hz or more was obtained in a relatively low frequency range from 25 to 60 Hz. The developed device can output sufficiently high AC voltage to be rectified by PN-junction diodes and thus to charge electricity to a capacitance with the vibration of 3 mG excitation in a frequency range from 25 to 60 Hz.

By adjusting the initial position of the electrodes, the frequency bandwidth could be further extended to 95 Hz. In the following sections, we discuss the electrostatic design theory, fabrication, and characterization of the newly developed energy harvester.

## 2. Theory for Electret Soft-spring Effect

The electrostatic soft-spring effect is used in this work to widen the frequency bandwidth of a vibrational energy harvester. The soft-spring effect is caused by the electrostatic attractive force acting on the electrodes that are pulled in the direction opposite to the mechanical restoring force of the spring. An analytical model for the electrodes is shown in Fig. 1. Protrusion structures are arrayed on the fixed and the movable electrodes with a small gap so that they would glide over each other without mechanical friction. The movable electrode is suspended by elastic springs, constituting a mechanical oscillator at a specific resonant frequency.

Despesse *et al.* reported the fabrication of a similar tunable comb structure with small protrusions by using electroplated nickel.<sup>(22)</sup> In their work, the periodic protrusions were used to cause a cyclic change of capacitance as a function of the displacement, but the effect on the effective spring constant was not considered.

Murotani and Suzuki also proposed an electret MEMS energy harvester with periodic electrodes that give bistability to a comb drive vibrator.<sup>(23)</sup> They simulated the nonlinear performance of the comb drive energy harvester aided by the bistability of the periodic electrodes.

Different from their work, we used silicon as a material so that the thermally grown oxide was turned into a built-in electret skin that could be directly used as a power-generating mechanism through the electrostatic induction current.<sup>(24–26)</sup> At the same time, we found that the periodic substructures on the electrodes are essential for altering the behavior of the energy harvester.

The electrostatic capacitance between the electrodes is a periodic function of the displacement, as schematically illustrated in Fig. 2, where  $L$  is the pitch of the electrode teeth.

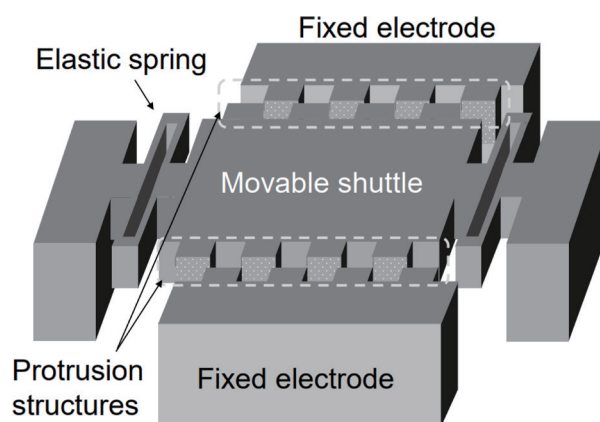


Fig. 1. Analytical model for a vibration energy harvester.

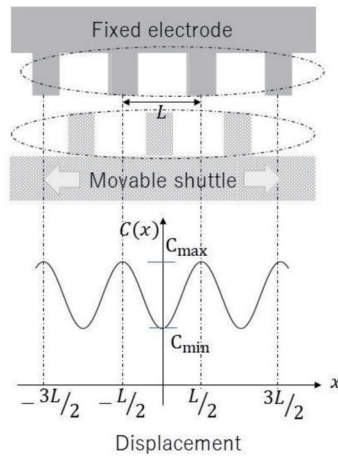


Fig. 2. First-order capacitance model with respect to the displacement of a movable electrode.

Although a precise function should be considered with the higher-order Fourier series depending on the electrode shapes, we took only the first-order function for simplicity of the analysis, as it has the most significant effect on the characteristics of the energy harvester.

By using the parameters depicted in Fig. 2, the capacitance is written as a function of the displacement  $x$  as

$$C(x) = \frac{C_{max} + C_{min}}{2} - \frac{C_{max} - C_{min}}{2} \cos\left(\frac{2\pi}{L}x\right) = C_a - C_b \cos\left(\frac{2\pi}{L}x\right), \quad (1)$$

where the effect of parasitic capacitances is included in  $C_a$  and  $C_b$ .

Since the electrostatic potential defined by the electret voltage  $E_{elec}$  can lower the profile of the total potential, we write the total potential energy  $U_t$  and the static force  $F_s$  respectively as

$$U_t = \frac{1}{2}kx^2 - \frac{1}{2}C(x)E_{elec}^2, \quad (2)$$

$$F_s = -\frac{\partial U_t}{\partial x}, \quad (3)$$

where  $k$  is the elastic constant of the suspensions.

Using the device dimensions in this work listed in Table 1,  $U_t$  and  $F_s$  are calculated as functions of the displacement and shown in Fig. 3; we used three different potential energy levels for the electret: (a) 50 V as a negligible level, (b) 120 V as a medium level, and (c) 200 V as an excessive level. The potential energy bottom around a small displacement is magnified in Fig. 3(d).

As can be seen in Fig. 3(a), the electrical field does not visibly affect the potential energy distribution when the electret voltage is as low as 50 V. In such a case, the net stiffness force

Table 1

Device parameters used in this work.

Parameter	Symbol	Value
Electrode pitch	$L$	40 $\mu\text{m}$
Maximum capacitor value	$C_{max}$	80 pF
Minimum capacitor value	$C_{min}$	44 pF
Elastic constant	$k$	1200 N/m

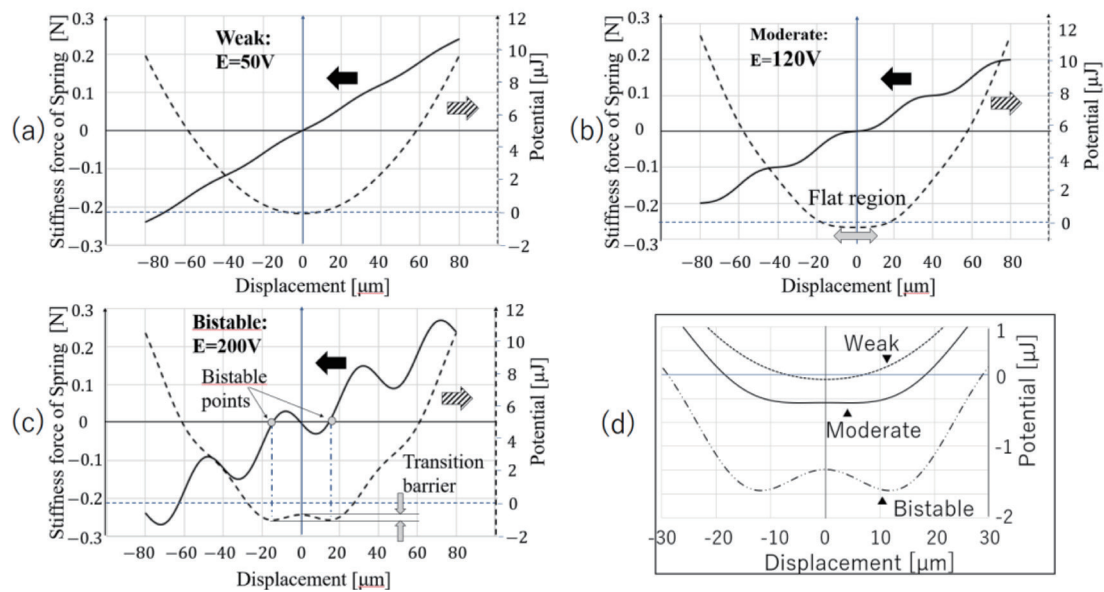


Fig. 3. (Color online) Calculated total potential energy and force for the electret voltages of (a) 50, (b) 120, and (c) 200 V. (d) Magnified potential view of the three cases.

remains almost proportional to the displacement, and thus the oscillating system is approximately modeled as a harmonic oscillator. When the electret potential is increased to 120 V, the stiffness curve begins to show staircase structures, as shown in Fig. 3(b). At the same time, the potential curve shows a plateau at the bottom near zero, within which the oscillator becomes free to oscillate owing to the weak constraining force. When the electret potential is further increased to 200 V, the local potential bottom splits into two different places, as shown in Fig. 3(c). Once the oscillator is trapped in such a local minimum, a small excitation vibration would not effectively agitate the oscillation between the local minima. Therefore, the electret potential should be set at a moderate voltage level such that the potential bottom would have a wide flat region with a small activation energy barrier. From the force curve point of view in Fig. 3, the slope near the initial point becomes very small; this means that the restricting force for the movable electrodes becomes small. Hence, the oscillator causes a relatively large displacement even under low-level acceleration.

Lagrange's equations are used to estimate the equivalent elastic spring constant. Taking the voltage applied to the capacitance  $e$  and the vibration velocity  $v$  as variables for generalized velocities, Lagrange's function  $L_a$  and the dissipation function  $\Gamma$  are respectively written as

$$L_a = \frac{1}{2} m v^2 + \frac{1}{2} C(x) e^2 - \frac{1}{2} k x^2, \quad (4)$$

$$\Gamma = \frac{1}{2} r_f v^2, \quad (5)$$

where  $m$  is the mass of the suspended body,  $k$  the total elastic constant of the springs, and  $r_f$  the damping coefficient.<sup>(27)</sup> From these functions, one can derive the equations of motion in terms of the mechanical force  $f$  and the electrical current  $i$  respectively as

$$f = \frac{d}{dt} \left( \frac{\partial L_a}{\partial v} \right) - \frac{\partial L_a}{\partial x} + \frac{\partial \Gamma}{\partial v} = m \frac{dv}{dt} + kx + r_f v - \frac{\pi}{L} C_b e^2 \sin \left( \frac{2\pi}{L} x \right), \quad (6)$$

$$i = \frac{d}{dt} \left( \frac{\partial L_a}{\partial e} \right) + \frac{\partial \Gamma}{\partial e} = \frac{2\pi}{L} C_b e \sin \left( \frac{2\pi}{L} x \right) v + C(x) \frac{de}{dt}. \quad (7)$$

From Eq. (6), the restoring force  $F_R$  of the mechanical system is written as a function of the displacement  $x$  and the capacitance voltage  $e$  as

$$F_R(x, e) = kx - \frac{\pi}{L} C_b e^2 \sin \left( \frac{2\pi}{L} x \right). \quad (8)$$

On the basis of equivalent linearization, we presume that the solution of Eq. (6) is represented by

$$x = a \cos \theta, \quad \theta = \omega t - \alpha, \quad (9)$$

where  $a$  is the amplitude of the vibration,  $\omega$  the angular velocity,  $t$  the variable of time, and  $\alpha$  a constant for phase.

We also presume that the electret voltage is sufficiently high to keep  $e$  almost constant, and therefore, the fundamental order of the restoring force is written as

$$F_R(x) = kx - \frac{\pi}{L} C_b E_{elec}^2 \sin \left( \frac{2\pi}{L} x \right) = A \cos \theta, \quad (10)$$

where  $E_{elec}$  is the electret voltage. The parameter  $A$  is a constant that can be determined by a solution of the first-order coefficient of the Fourier series in Eq. (10), that is,

$$\begin{aligned} A &= \frac{1}{\pi} \int_0^{2\pi} \left[ ka \cos \theta - \frac{\pi}{L} C_b E_{elec}^2 \sin \left( \frac{2\pi}{L} a \cos \theta \right) \right] \cos \theta d\theta \\ &= ka - \frac{2\pi}{L} C_b E_{elec}^2 J_0 \left( 1, \frac{2\pi}{L} a \right), \end{aligned} \quad (11)$$

where  $J_0 \left( 1, 2\pi a / L \right)$  is a Bessel function of the first kind.

From Eqs. (9) and (10),  $F_R(x)$  is simply written as

$$F_R(x) = A \cos \theta = \frac{A}{a} x. \quad (12)$$

Therefore, the effective spring constant  $k_{eff}$  is written as

$$\begin{aligned} k_{eff} &= k - \frac{2\pi}{aL} C_b E_{elec}^2 J_0 \left( 1, \frac{2\pi}{L} a \right) \\ &= k - 2 \left( \frac{\pi}{L} \right)^2 C_b E_{elec}^2 \left[ 1 - \frac{1}{2} \left( \frac{\pi}{L} a \right)^2 + \frac{1}{12} \left( \frac{\pi}{L} a \right)^4 - \frac{1}{144} \left( \frac{\pi}{L} a \right)^6 + \dots \right]. \end{aligned} \quad (13)$$

Figure 4 shows the effective spring constant as a function of vibration amplitude, which was calculated using Eq. (13) for the electret voltage of 120 V and device parameters listed in Table 1. The elastic constant around the initial position of the movable electrode is estimated to be 190 N/m, which agrees well with the value calculated from the slope of the force curve shown in Fig. 3(b). In a large amplitude range, the effective spring constant becomes asymptotically close to the structural spring constant, which is the average slope of the force curve.

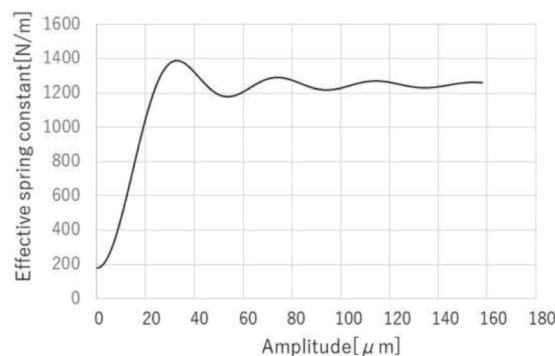


Fig. 4. Calculated effective spring constant as a function of vibration amplitude by using the method of equivalent linearization.

The effective spring constant is related to the average curvature of the potential curve within the vibration amplitude, as shown in Fig. 5. For instance, the bold curve shown in Fig. 5(a) is the vibration trajectory on the total potential when the oscillation amplitude is  $10\ \mu\text{m}$ ; compared with the mechanical potential of the spring shown by the dotted curve, the total potential curve is slightly flatter than that of the mechanical potential. For the oscillation amplitude of  $30\ \mu\text{m}$  shown in Fig. 5(b), on the other hand, the total potential and the mechanical potential are almost alike but slightly sharp at around  $\pm 20\ \mu\text{m}$ . According to the equivalent linearization theory, the calculated spring constant corresponds to the curvature approximated by the quadratic function within the considered range. Therefore the flat area of the potential curve within the small displacement ( $\pm 10\ \mu\text{m}$ ) corresponds to a small spring constant, whereas that for a large displacement ( $\pm 20\ \mu\text{m}$ ) leads to an effective spring constant slightly larger than the mechanical one.

In the transient zone, the effective elastic constant increases with increasing amplitude; this transient range corresponds to the stroke within a pitch of the electrode protrusions, indicating that a nonlinear behavior can thus be engineered by adjusting the electrode shapes and the electret potential. Within the small displacement range, a wide-band frequency response is expected.

### 3. Effect of Initial Electrode Position on Nonlinear Frequency Response

The effect of the initial position of the movable electrode on the nonlinearity is investigated in this section. Figure 6 shows three representative initial positions of the movable electrodes with respect to the fixed ones. We classified three models on the basis of the spatial phase of the mutual position of the opposing protrusion structure.

Figure 6(a) shows the fundamental model with out-of-phase electrodes analyzed in the previous section. This model is extended to have a modulation term that depends on the initial mutual position of the electrode pairs. Figures 6(b) and 6(c) show the analytical models for the half-out-of-phase and in-phase comb electrodes, respectively. Equation (1) is rewritten as

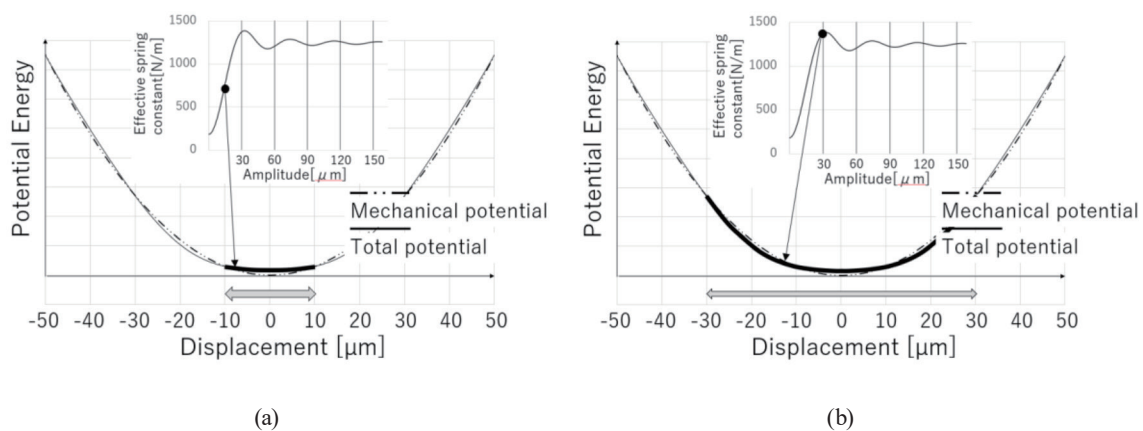


Fig. 5. Effective spring constant in relation to the average curvature of the total potential energy curve.

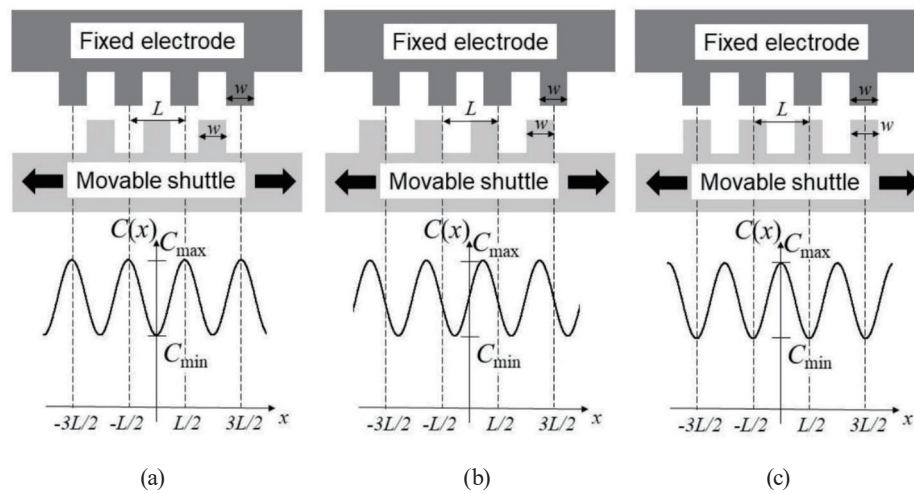


Fig. 6. Illustrations of initial positions of the movable electrode with respect to the fixed one. (a) Out-of-phase, (b) half-out-of-phase, and (c) in-phase arrangements.

$$C(x) = C_a - C_b \cos \left\{ \frac{2\pi}{L} (x + x_0) \right\}, \quad (14)$$

where  $x_0$  is the initial position of the movable electrode.

Figure 7 shows the calculated potential energies and attracting force acting on the movable electrode for the three initial positions. Different from the out-of-plane configuration in which the curvature at the potential bottom becomes smaller than the parabolic mechanical potential, the potential bottom becomes deeper for the in-plane configuration because the electrostatic force strongly attracts the movable part. Reflecting the potential shape, the slope of the force curve at the bottom is also steeper than that of the mechanical force curve. In contrast to the out-of-phase and in-plane configurations, the potential shape of the half-out-of-plane configuration is more asymmetric and the equilibrium point slightly shifts from the middle point of  $L/2$ . As shown in Fig. 5, the effective spring constant is dependent on the potential curvature. When the oscillation is small for the in-plane configuration, the device is expected to have a frequency response in a range higher than the natural resonant frequency. On the other hand, as shown in Fig. 7(d), the potential curvature near the bottom in the half-out-of-plane model is almost the same as that of the mechanical one, suggesting that the frequency response will be almost linear. To simulate the frequency response, we derive the time development differential equations for displacement  $x_n$ , short-circuit current  $i_n$ , and open-circuit voltage  $e_n$  from Eq. (4), where the subscript  $n$  represents the step number of time durations, as

$$x_{n+1} = \frac{\Delta t^2}{m + r_f \Delta t} \left\{ \frac{m(2x_n - x_{n-1})}{\Delta t^2} - kx_n + \frac{r_f x_n}{\Delta t} + \frac{\pi}{L} C_b (E + e)^2 \sin \left[ \frac{2\pi}{L} (x_n + x_0) \right] + ku_n + r_f \dot{u}_n \right\}, \quad (15)$$

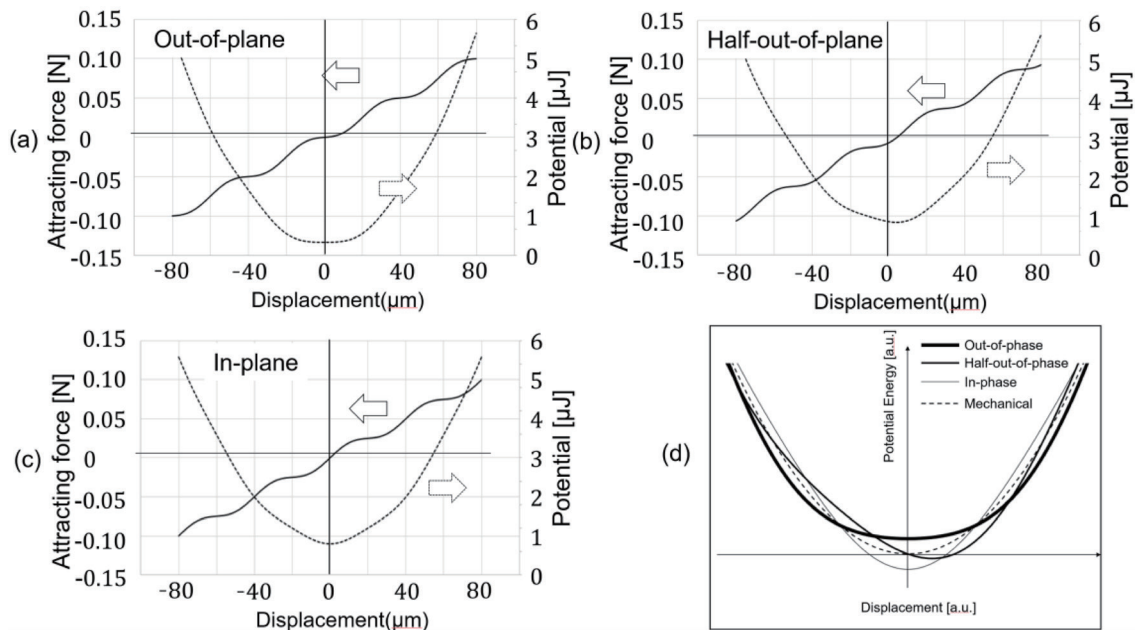


Fig. 7. Calculated potential energy and attractive force acting on the movable electrode for the three initial positions of (a) out-of-phase, (b) half-out-of-phase, and (c) in-phase positions. (d) Magnified view of the potential energy difference for the three initial positions. The potential of the mechanical spring is plotted with the dashed curve as a reference.

$$i_{n+1} = \frac{-EC_b}{\Delta t} \left\{ \cos \left[ \frac{2\pi}{L} (x_{n+1} + x_0) \right] - \cos \left[ \frac{2\pi}{L} (x_n + x_0) \right] \right\}, \quad (16)$$

$$e_{n+1} = e_n + C_b (E + e_n) \left\{ \cos \left[ \frac{2\pi}{L} (x_{n+1} + x_0) \right] - \cos \left[ \frac{2\pi}{L} (x_n + x_0) \right] \right\} / \left\{ C_a - C_b \cos \left[ \frac{2\pi}{L} (x_n + x_0) \right] \right\}, \quad (17)$$

where  $u$  is the excitation displacement and  $\dot{u}$  is its time derivative, i.e., the excitation velocity. The estimation of the open-circuit voltage and short-circuit current is essential to determine the output impedance. The short-circuit current determines the ability to charge a storage capacitor, whereas the open-circuit voltage indicates its maximum reachable level.

Simulation results of frequency responses were obtained by numerically sweeping up and down the excitation frequency in the simulation model. The actual parameters used in the simulations are listed in Table 2. In the linear electrostatic actuator theory,<sup>(27)</sup> output current is proportional to the vibration velocity, and its coefficient is referred to as a force factor. The product of force and vibration velocity, the power, can also be written as the electric product of voltage and current. The output voltage is proportional to the force and thus reciprocal to the

Table 2  
Simulation parameters.

Parameter	Symbol	Value
Electrode pitch	$L$	40 $\mu\text{m}$
Maximum capacitor value	$C_{max}$	47 pF
Minimum capacitor value	$C_{min}$	35 pF
Elastic constant	$k$	1248 N/m
Proof mass	$m$	$8.0 \times 10^{-3}$ kg
Damping coefficient	$r_f$	$3.16 \times 10^{-2}$ Ns/m
Electret voltage	$E$	120 V

force factor. In this work, we presume an excitation acceleration of as small as a few mG and the force factor value of  $1 \times 10^{-4}$  C/m, and we designed a proof mass of 8 g to make the output voltage high enough to be rectified by a diode bridge. In addition, the parameter  $x_{n=0}$  was set to 0  $\mu\text{m}$  for out-of-phase, 10  $\mu\text{m}$  for half-out-of-phase, and 20  $\mu\text{m}$  for in-phase models. The excitation displacement  $u$  was determined by the excitation acceleration of 3 mG using the relation of acceleration  $a_{acc} = \omega_0^2 u$ .

Figure 8 shows the simulation results of short-circuit current and open-circuit voltage under three different initial conditions of comb fingers, i.e., (a) and (b) for the out-of-phase, (c) and (d) for the half-out-of-phase, and (e) and (f) for the in-phase configurations. We used the normalized frequency  $f_c$ , with the resonant frequency being  $f_c = 1$ .

When the initial position of the electrodes was out-of-phase, as schematically shown in Fig. 6(a), the frequency responses of both short-circuit current and open-circuit voltage started to increase in the low frequency range ( $f_c \geq 0.85$ ), which is considerably lower than the resonance, as shown in Figs. 8(a) and 8(b); the oscillation stroke became large towards its resonance at  $f_c \sim 1$ . At first glance, it looked like a typical behavior of a hard-spring effect because the resonant spectrum inclines toward the higher frequency side, but the peak oscillation in practice took place at around the designed resonance. Therefore, it should be interpreted that the effective resonance of the system was first down-shifted by the virtual soft-spring effect associated with the electrostatic attractive force that pulled the movable electrodes in the direction of motion.

As shown in Fig. 5, the total potential is modulated by the electrostatic potential. However, under a large displacement condition, the total potential becomes close to the inherent mechanical potential. This tendency is reproduced in the simulation result; when the oscillation grows large to cover the multiple comb tips, the effect of the electrostatic attractive force becomes moderate, and the oscillation starts to show its own resonance.

When the initial condition was changed to half-out-of-phase, as schematically shown in Fig. 6(b), the nonlinearity from the electrostatic attractive force was lowered, and the oscillation behavior resembled that of a linear system shown in Figs. 8(c) and 8(d); under this condition, the peak amplitude was found at  $f_c \sim 1$  as designed.

When the initial condition was finally changed to in-phase, as schematically shown in Fig. 6(c), the resonance was shifted towards the higher frequency range at around  $f_c \sim 1.1$ , as shown in Figs. 8(e) and 8(f). Once again, this phenomenon resembled that of a soft-spring effect at first glance because of the peak inclining towards the low-frequency side. However, note that

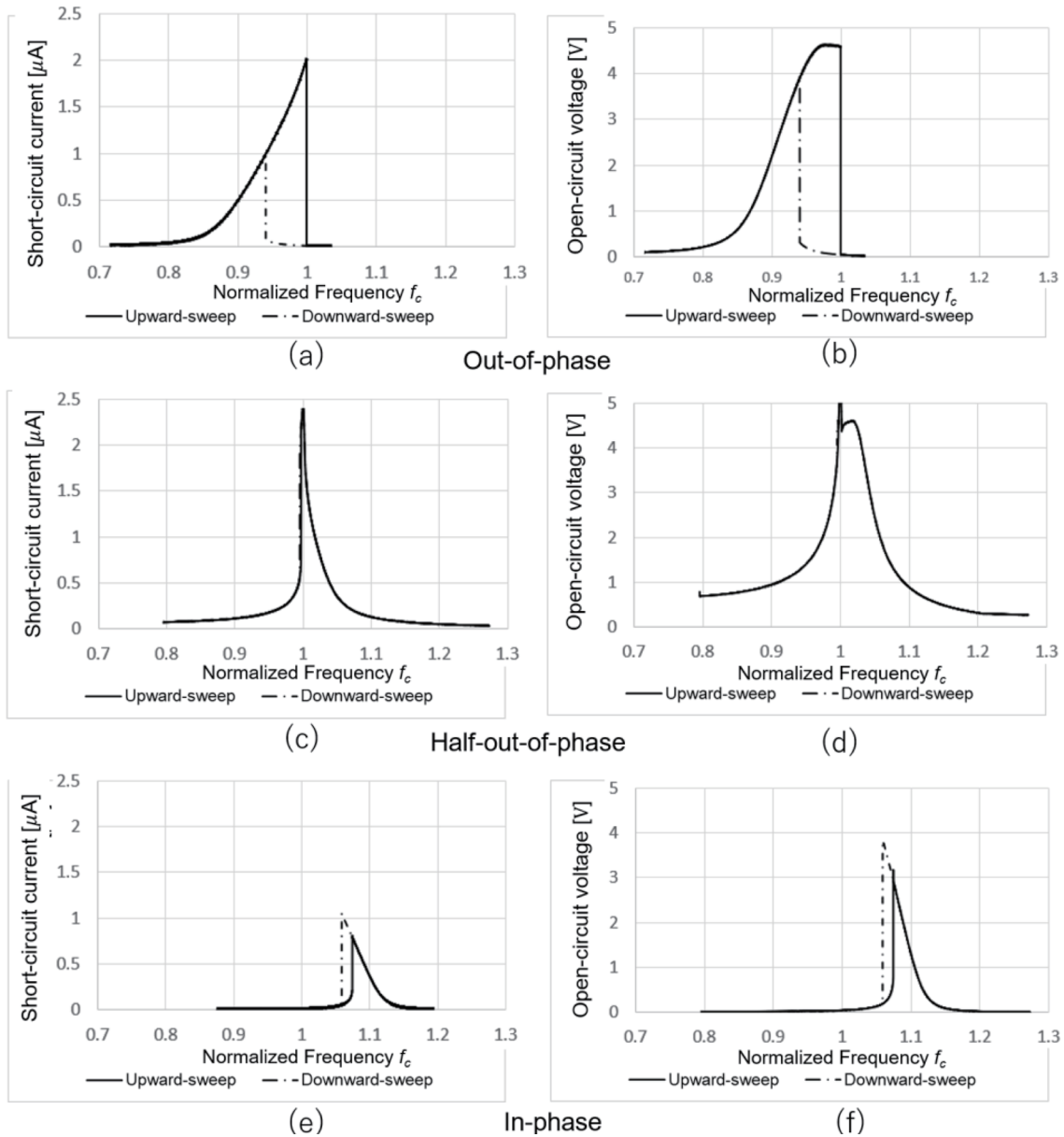


Fig. 8. Simulation results of (left) short-circuit current and (right) open-circuit voltage for the (a) and (b) out-of-phase configuration, (c) and (d) half-out-of-phase configuration, and (e) and (f) in-phase configuration devices.

the actual resonance took place at a frequency higher than the designed resonance. This could also be understood that the effective resonance of the system was up-shifted by the virtual hard-spring effect associated with the electrostatic constraint force applied to keep the comb fingers aligned to each other. As the oscillation grew, the electrode motion became less constrained and started to reveal its own resonance towards  $f_c \sim 1$ . Nevertheless, the oscillation collapsed on the way to resonance, because the excitation frequency was changed excessively fast in this simulation that was programmed to finish in a finite time.

In the same manner as used to derive Eq. (13), the effective constant for the in-phase configuration is written as

$$k_{eff} = k + \frac{2\pi}{aL} C_b E_{elec}^2 J_0 \left( 1, \frac{2\pi}{L} a \right), \quad (18)$$

where the second term is added to express the hard-spring effect. The movable electrode is attracted to the opposite electrode by the electrostatic force, deepening the valley of the elastic potential. This effect is reflected in the enhancement of the net potential curvature in a small displacement range, occasionally making the second term greater than the mechanical spring constant.

#### 4. Fabrication of Vibrational Energy Harvester

The harvester device used in this study was composed of 1200 pairs of electrode protrusions arranged on 40 pairs of interdigitated comb electrodes made of silicon. Figure 9 shows the entire top-view layout of the photomask, with a close-up view of the protrusion electrodes. The device was developed using an SOI wafer with a 300- $\mu\text{m}$ -thick top silicon layer, a 2- $\mu\text{m}$ -thick buried oxide (BOX) layer, and a 500- $\mu\text{m}$ -thick silicon substrate. The dimensions of one protrusion were 20  $\mu\text{m}$  wide and 100  $\mu\text{m}$  long, placed at every 40  $\mu\text{m}$ . The gap between opposing electrodes was 20  $\mu\text{m}$ .

The fabrication sequence is schematically shown in Fig. 10. In step (1), we prepare an SOI wafer covered with a 200-nm-thick silicon nitride (SiN) layer made by low-pressure chemical vapor deposition (LPCVD). It is patterned in step (2) to define the area for the contact pads. In step (3), the device structures are formed in the SOI layer by DRIE using the Bosch technology. On the reverse side, a through-hole is created also by the DRIE in step (4). In step (5), the mechanically movable parts are released by the selective removal of the BOX layer in HF acid. Having prepared such suspended microstructures, we then use a KOH aqueous solution for wet oxidation in step (6) to produce a potassium-rich silicon oxide film on the device surfaces except the protected areas under the SiN patterns. Such areas are opened for electrical contact later in step (7) by the selective removal of the SiN patterns by RIE using  $\text{CF}_4$  reactive gas.

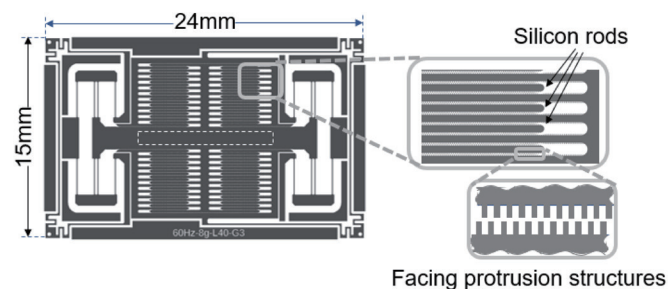


Fig. 9. Photomask patterns of the vibrational energy harvester. Electrode combs have yet smaller protrusions on the side walls to periodically alter the electrostatic capacitance.

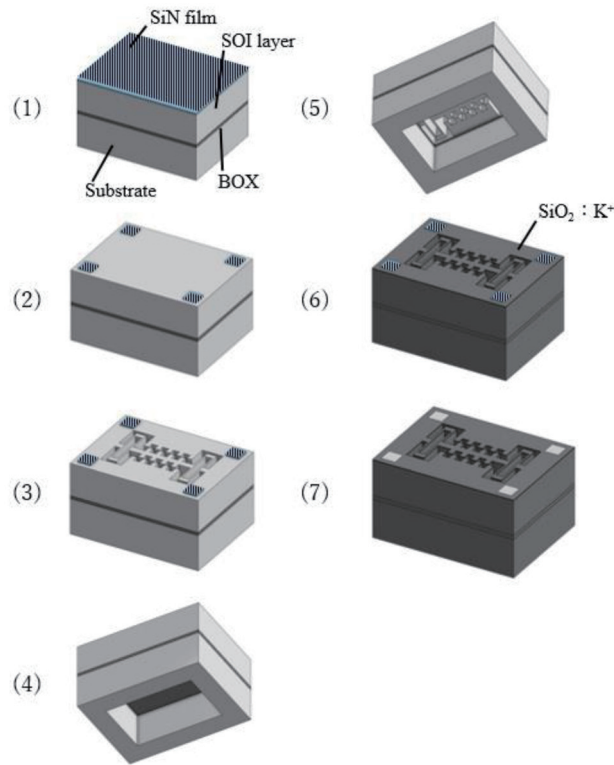


Fig. 10. (Color online) Schematic of the device fabrication sequence.

After the completion of the device structures, we used an electrical charging process called the biased-temperature (BT) process. The device was annealed to approximately 600 °C on a heater, and a dc voltage of 120 V was applied between the electrodes, thereby leaving permanent electrical charges in the silicon oxide film on the anode side; the details of the charging process have been reported elsewhere.<sup>(25)</sup> Finally, we put an 8 g mass made of tungsten on the movable part; a 16-mm-long, 6-mm-wide, and 3.5-mm-high tungsten block and a 16-mm-long, 2-mm-wide, and 2.5-mm-high tungsten block were stacked and fixed with epoxy resin to make a convex cross-sectional block. Then, we manually placed it on the center area of the fabricated device and fixed it with an adhesive.

Figure 11 shows a photograph of the developed device; the total device dimensions were 15 mm wide, 24 mm long, and 7 mm thick, including the add-on mass. Since the spring constant of the vertical direction is estimated to be about 45000 N/m, the deflection, caused by gravity, of the proof mass is expected to be 1.75 μm; this will be negligible for the operation of the device.

As described above, we utilized the silicon oxide film as an electret material. Figure 12 shows an Arrhenius plot of the -1 dB voltage degradation lifetime of the electret film we developed. The high-temperature test was conducted in a vacuum chamber of less than  $1 \times 10^{-3}$  Pa. The lifetime showed over 100 years at room temperature, exhibiting high reliability as a standard electronic component. However, as it is very sensitive to humidity, like other nonorganic electret materials, a package to prevent exposure to humidity is usually required.

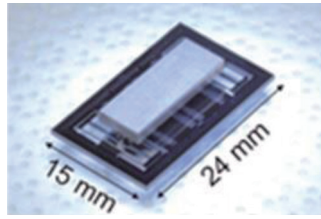


Fig. 11. (Color online) Photograph of the developed vibration energy harvester. An 8 g tungsten mass is attached to the movable electrode.

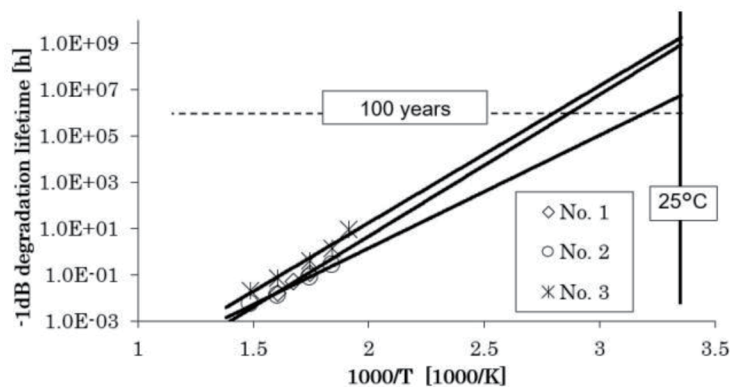


Fig. 12. Arrhenius plot of  $-1$  dB voltage degradation lifetime of the electret film made of silicon oxide film. Three samples were tested by high-temperature acceleration examination in vacuum.

## 5. Characterization

### 5.1 Out-of-phase electrodes

We have fabricated several devices by the process described in the previous section, but here, we first tested one of the devices to investigate whether it could be tuned to have the potential curve shown in Fig. 3(b).

By using the measurement setup shown in Fig. 13, the frequency characteristics of short-circuit current and open-circuit voltage were measured on the device with the out-of-phase electrodes. The short-circuit properties can be interpreted as the intrinsic kinetic performance of the harvester because the effect of the electrostatic force associated with the potential difference across the electrodes is eliminated under this condition. The open-circuit voltage, on the other hand, includes the effect of the electrostatic force associated with the voltage generated within the chip by the energy harvesting process. In a simplified linear model, the motion equation derived from Eq. (6) is written as

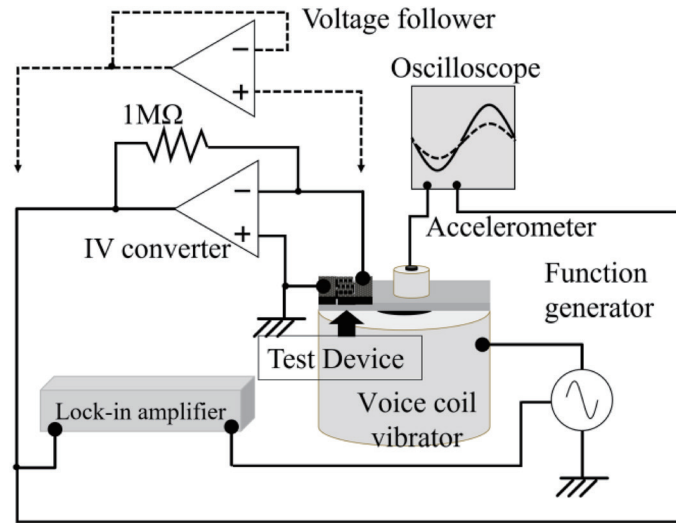


Fig. 13. Measurement setup for the characterization of the vibration energy harvester. An  $I$ - $V$  converter was used to obtain the short-circuit current, while a voltage follower was used for the open-circuit voltage.

$$f = j\omega mv + r_f + kx - \frac{2\pi^2}{L^2} C_b E_{elec}^2 \cos\left(\frac{2\pi}{L} X\right) x - \frac{2\pi}{L} C_b E_{elec} \sin\left(\frac{2\pi}{L} X\right) e, \quad (19)$$

where  $j$  is the imaginary unit ( $j^2 = -1$ ),  $X$  represents the initial displacement caused by the electret bias voltage, and  $\omega$  is the angular velocity.  $x$  and  $e$  are alternating displacement and voltage with small amplitude, respectively.

The electrical linear equation under the open-circuit condition is given by

$$0 = i = \frac{2\pi}{L} C_b E \sin\left(\frac{2\pi}{L} X\right) v + j\omega C_X e, \quad (20)$$

where  $C_X$  is the initial capacitance value at the initial displacement  $X$ .

Substituting Eq. (20) into Eq. (19) and eliminating the variable  $e$ , we obtain the total effective spring constant as

$$k_{eff} = k - \frac{2\pi^2}{L^2} C_b E_{elec}^2 \cos\left(\frac{2\pi}{L} X\right) + \frac{4\pi^2}{L^2} \frac{C_b^2}{C_X} E_{elec}^2 \sin^2\left(\frac{2\pi}{L} X\right). \quad (21)$$

The third term is the feedback effect caused by the output voltage generated under the open-circuit condition. Under the out-of-phase condition, the initial displacement  $X$  is assumed to be almost zero. Hence, the contribution of the feedback effect is considered to be negligible.

As schematically shown in Fig. 13, the device under test was put on a voice-coil vibrator to apply the sinusoidal acceleration; a current–voltage ( $I$ – $V$ ) converter with a  $1\text{ M}\Omega$  feedback resistance was used to read out the short-circuit current, while a voltage follower was used to monitor the open-circuit voltage. In both cases, a lock-in amplifier (NF corporation LI5660) was used to plot the data as a function of the excitation frequency. An accelerometer (EMIC Corporation model 760-B) was also attached to the voice-coil vibrator to simultaneously monitor the excitation vibration during the measurement of electrical characteristics. The root-mean-square (rms) values of the output signals were observed on an oscilloscope (Keysight DSOX3014T) as well as records of the waveforms of the acceleration and output electrical signals. We used a mathematic function of the oscilloscope to automatically calculate the rms values. The excitation frequency was swept up and down in the range between 20 and 60 Hz.

Figures 14(a) and 14(b) respectively show the frequency response of the short-circuit current and the open-circuit voltage excited by 3 mG vibration. While the comb-drive devices having no protrusion structures on the comb-fingers exhibited a linear resonant peak with a bandwidth of less than 5 Hz, as reported elsewhere,<sup>(28)</sup> a nonlinear effect was clearly observed in the frequency response with a large hysteresis loop in this work; the signal became visible in a relatively wide range from 22 to 58 Hz in the swept-up sequence, while it showed a small peak at around 30 Hz in the swept-down sequence. The spring constant of the suspensions used in this work was calculated to be 1200 N/m when no electrostatic effect was taken into account. By considering the added mass of 8 g, the mechanical resonance was expected at around 61.6 Hz, which was beyond the upper limit of the spectrum. According to our theoretical model, on the other hand, the spring constant effectively decreased to 190 N/m owing to the electrostatic effect, suggesting a resonant frequency of 24.5 Hz, which agrees well with the characteristic frequency at the root of the spectrum shown in the figure. Therefore, the theoretical model in this work is considered to give a rule-of-thumb approximation to design the frequency response. For further refinement of the model, the distributed mass of the silicon structures as well as the fixing resin should be considered. The side etching effect of DRIE should also be considered, as it could have thinned the final width of the suspensions, lowering the resonant frequency.

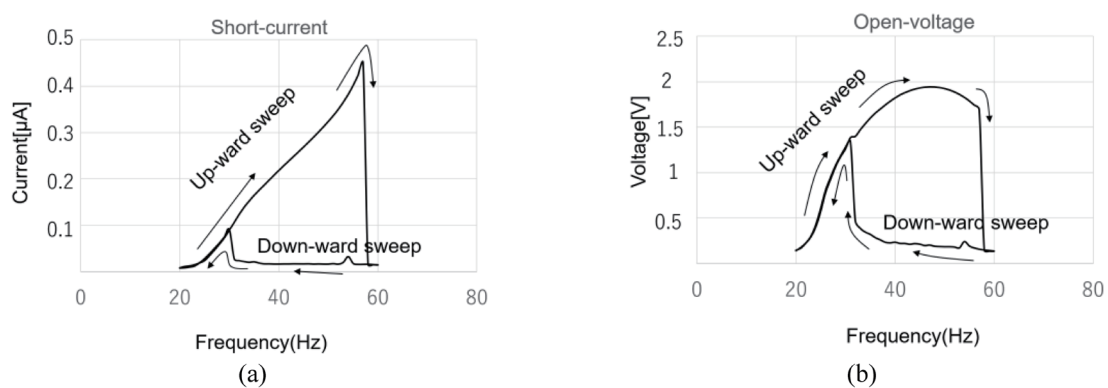


Fig. 14. Frequency responses of energy harvester under 3 mG excitation condition. (a) Short-circuit current and (b) open-circuit voltage.

As shown in Fig. 14, the experimentally obtained spring constant appears to have been softened from the theoretical value owing to the bias voltage effect,<sup>(16)</sup> because the resonance is excited at a frequency considerably lower than the designed mechanical resonance. As the excitation frequency increases, the spring constant returns to its original value. The shape of the spectrum reminds us of a hard-spring effect caused by the stress stiffening of the spring under a large deformation condition. Nevertheless, the elasticity of the spring in this work is considered to remain in a linear region by considering the size of the stroke with respect to the suspension dimensions. Therefore, the shape of the spectrum must be interpreted by using the potential curve shown in Fig. 3(b).

When the excitation frequency is considerably lower than the mechanical resonant frequency, the stroke of the movable electrode remains in the small flat region of the potential shown in Fig. 3(b), resulting in an effectively smaller spring constant than its true value defined by the dimensions. When the excitation frequency becomes close to the mechanical resonance, the stroke of the movable part gradually increases to follow the parabolic potential curve of  $kx^2/2$ , thereby revealing its true spring constant  $k$ . The effective spring constant can never be greater than this  $k$ , and thus the eigen frequency inherent to the mass and the spring is the upper limit of oscillation that could be sustainably excited. At any frequencies higher than this, the oscillation finally collapses.

For a more detailed study, we compared the short-circuit current and the open-circuit voltage, measured at 30 Hz with a small vibration of 2 mG<sub>rms</sub> and the results are shown in Fig. 15, which shows a part of a long sequence of waveforms and therefore, the initial values of the current and voltages are not null. The frequencies of both outputs are twice as high as the excitation frequency, as shown in Figs. 15(b) and 15(c), because the initial position of the protrusion electrodes was symmetrically staggered with their tips aligned to the valleys and they produce two peaks of the same polarity in a single cycle of oscillation. Note that the peak values of the open-circuit voltage exceed 2 V at a frequency of more than 25 Hz far from the mechanical resonance and even the acceleration was as small as 2 mG, suggesting that the device can generate voltages high enough to be rectified by a typical diode at a frequency off the real resonance.

When excited by a 50 mG<sub>rms</sub> acceleration waveform at 56.6 Hz, as shown in Fig. 16(a), which was almost the resonance, the short-circuit current and the open-circuit voltage become more complex in shape, as respectively shown in Figs. 16(b) and 16(c). Each peak and bottom point in the short-circuit current corresponds the pitch (40 μm) of the protrusion electrode; therefore, counting such a number contained in a single envelope of oscillation, we estimate the mechanical stroke to be 240 μm.

A peak short-circuit current of 4.3 μA was observed at 50 mG<sub>rms</sub>, as shown in Fig. 16(b). Compared with that measured at 2 mG<sub>rms</sub> shown in Fig. 15(b), this is a 25-fold improvement, which is equal to the linear ratio of magnitudes between 50 mG<sub>rms</sub> and 2 mG<sub>rms</sub>. On the other hand, the open-circuit voltage does not show such a large contrast but it was 2.55 V for 2 mG<sub>rms</sub> and 3.25 V for 50 mG<sub>rms</sub>. Moreover, the peak current seems to be strongly dependent on the passing-by velocity of the electrodes, while the open-circuit voltage peaks for the 50 mG<sub>rms</sub> excitation are all at a similar level. By paying attention again to the difference between Figs. 14(a)

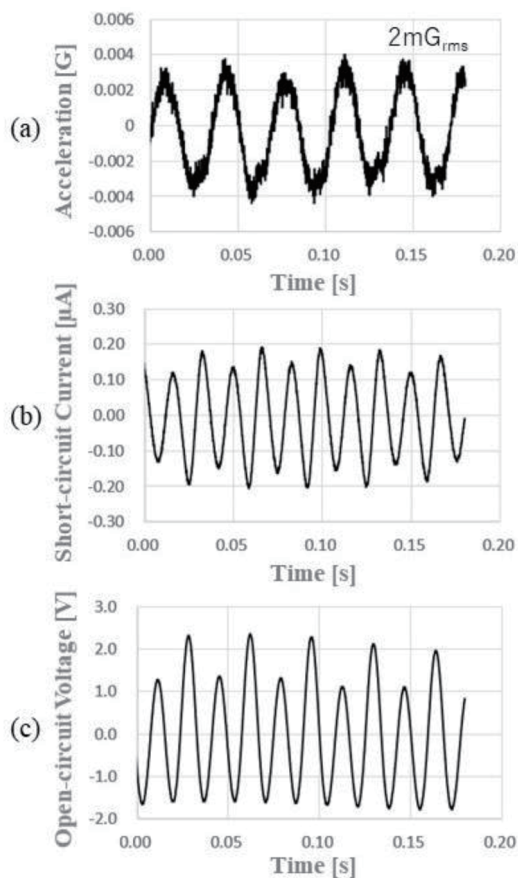


Fig. 15. Waveforms of short-circuit current and open-circuit voltage measured for a small acceleration of  $2 \text{ mG}_{\text{rms}}$  at 30 Hz.

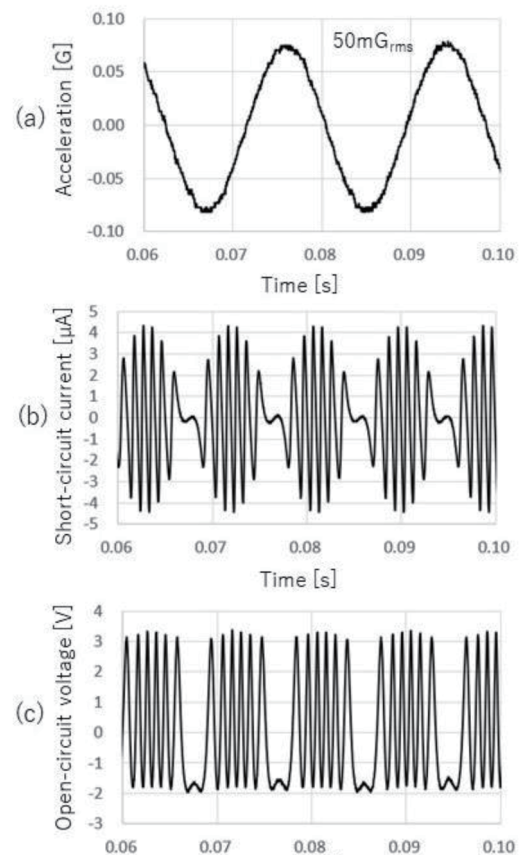


Fig. 16. Waveforms of (a) excitation acceleration, (b) short-circuit current, and (c) open-circuit voltage measured at a small acceleration of  $50 \text{ mG}_{\text{rms}}$  at 56.6 Hz.

and 14(b), we see a straight curve in the short-circuit current spectrum and a round peak in the open-circuit voltage spectrum. The difference between these behaviors is thought to have been caused by the voltage that is governed by the built-in electric field of the electrets.

We can also explain that the output impedance of the vibrational energy harvester is a function of vibration amplitude. From the phase difference between the output voltage and the current, the harvester is a two-port capacitive device. In a small amplitude range, where the overlap length between the electrode tips remains small, the output impedance is relatively high. At a large amplitude, on the other hand, the average overlap length becomes large and thus the impedance is low. As a result, the output peak voltage becomes almost constant, while the current peak is proportional to the vibration velocity.

Figure 17 shows the output power as a function of the load resistance when excited by an acceleration of 10 mG at 57.4 Hz. The output power was calculated by the rms value of the current flowing through the load resistances. We examined the maximum power at other frequencies and found that 57.4 Hz was the best condition to maximize the retrievable power. Peak power was observed at  $2 \text{ M}\Omega$ , which agrees well with the value calculated from the short-

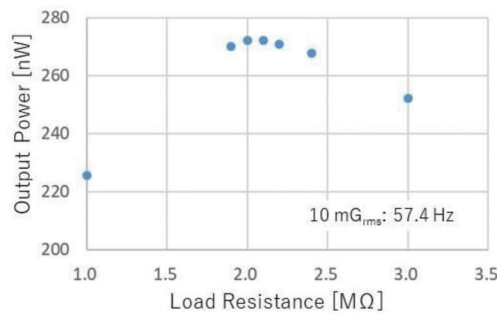


Fig. 17. (Color online) Output power as a function of the load resistance, excited by acceleration of 10 mG at 57.4 Hz.

circuit current of about 500 nA and the open-circuit voltage of about 1.1 V, that is,  $1.1 \text{ V}/500 \text{ nA} \sim 2.2 \text{ M}\Omega$ , as later shown in Fig. 21 in the next subsection.

According to the linear equivalent circuit theory of an electrostatic oscillator,<sup>(27)</sup> the output impedance is represented by the parallel connection of a capacitor between the electrodes and the resistance corresponding to the mechano-electric loss. The latter must include the electrical resistance of the material used, but the SOI wafer in this work had a very low resistivity (0.01  $\Omega\text{cm}$ ) and the total resistance of silicon was estimated to be 10  $\Omega$  or less, which is negligible compared with the overall impedance of the device.

Assuming the essential device volume of  $2.4 \times 1.5 \times 0.7 \text{ cm}^3$ , the normalized volumetric power density (NPD,  $\text{W}/\text{cm}^3/\text{G}^2$ ) of the device is about  $1.07 \text{ mW}/\text{cm}^3/\text{G}^2$ ; the device in this work has a relatively high power efficiency compared with those reported elsewhere.<sup>(28)</sup>

Figure 18 shows the fast Fourier transform (FFT) spectra of the short-circuit current and the open-circuit voltage when excited by a white noise signal that spans between 0 and 100 Hz. The rms value of the acceleration was tuned to either 10 mG or 20 mG. Note that frequencies in the output signals are found at even-number harmonics because the initial position of the movable electrodes is set to be symmetric with respect to the fixed electrodes for the out-of-phase configuration.

For the acceleration of 10 mG, the spectrum peaks are seen between 50 and 70 Hz for both current and voltage. For 20 mG, on the other hand, the peak frequency increases to 100 Hz, and higher order peaks become visible. This behavior is understood by considering again the effective elastic constant; for a small acceleration such as 10 mG, the stroke of the movable electrode remains small, and thus the effective elastic constant is small, as shown in Fig. 4. For a rather large acceleration such as 20 mG, on the other hand, the stroke, as well as the effective spring constant, becomes large, thereby shifting the resonant frequency towards the higher frequency side. At the same time, the increased stroke starts to cover multiple numbers of protrusions on the counter electrode, and thus the output signal contains more harmonic components, as shown by the FFT analysis. Note that the frequency response is changed solely by the excitation level without any conditioning electronics.

Figure 19 shows the result of a charging test of the 10 and 20 mG white-noise excitations via a full-wave rectification circuit. The voltage stored in a 15  $\mu\text{F}$  capacitance was monitored using a high-input-impedance voltage follower. From Bessel's inequality, that is,

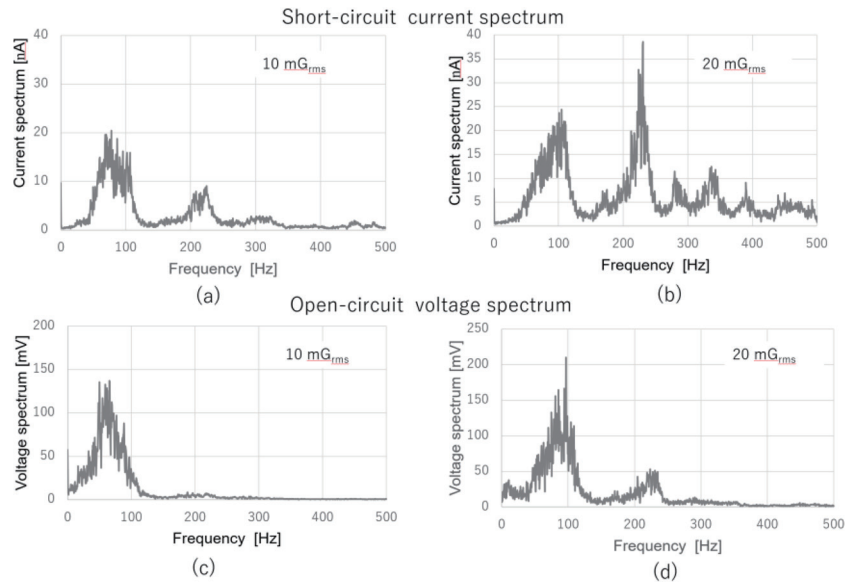


Fig. 18. FFT spectra of the short-circuit current excited by white-noise signal of (a) 10 mGrms and (b) 20 mGrms acceleration with 100 Hz bandwidth. FFT spectra of the open-circuit voltage excited by white-noise signal of (c) 10 mGrms and (d) 20 mGrms acceleration with 100 Hz bandwidth.

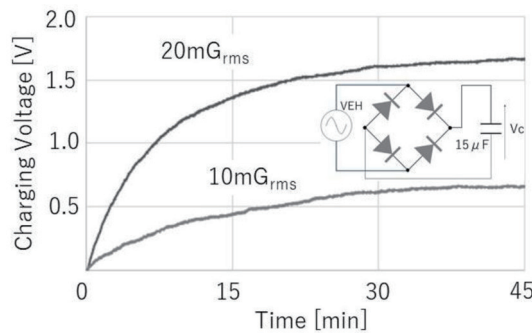


Fig. 19. Charging test of the 10 and 20 mGrms white-noise excitations via a full-wave rectification circuit stored in a capacitance of 15 μF.

$$\frac{1}{T} \int_0^T f(t)^2 dt \geq \sum_{n=1}^N |c_n|^2, \tag{22}$$

where  $f(t) = \sum_{n=1}^N c_n \exp(jn\omega t)$ , the RMS values of the open voltage derived from the FFT data are expected to be 0.90 V for 10 mG and 0.98 for 20 mG. The FFT data were an ensemble of 5 data with a 1 kHz sampling rate during 2 s but the charging tests were conducted for 45 min. In separate measurements, we obtained FFT data showing 0.57 V as the RMS value in a 10 mG open-circuit voltage experiments and over 1.3 V for 20 mG. Therefore, the final value of the charging voltage is expected to be around the RMS value of the open-circuit voltage if the leakage of the capacitance is sufficiently small compared with the charging current.

## 5.2 In-phase electrodes

To examine the frequency response that depends on the initial electrode position, as described in Sect. 3, we conducted electrical measurement by tilting the excitation shaker as shown in Fig. 20. The 8 g mass on the device was sufficiently large to experience the gravity of Earth to alter the initial position of the electrodes, depending on the tilt angle. Therefore, the mass can virtually alter the electrode design from the original out-of-phase to the in-phase configuration.

Figure 21 shows the open-circuit voltages and short-circuit currents at different shaker angles of 0 and 15°. Acceleration of the excitation vibration was 10 mG<sub>rms</sub>, which was monitored using

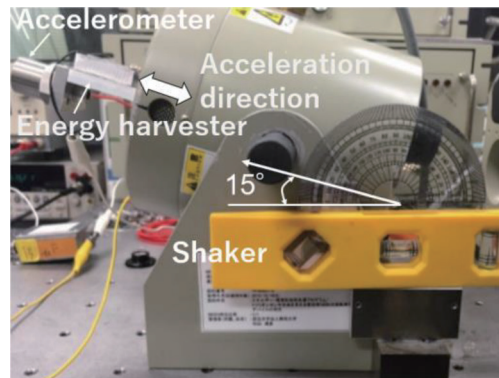


Fig. 20. (Color online) Photograph of the shaker tilted 15°.

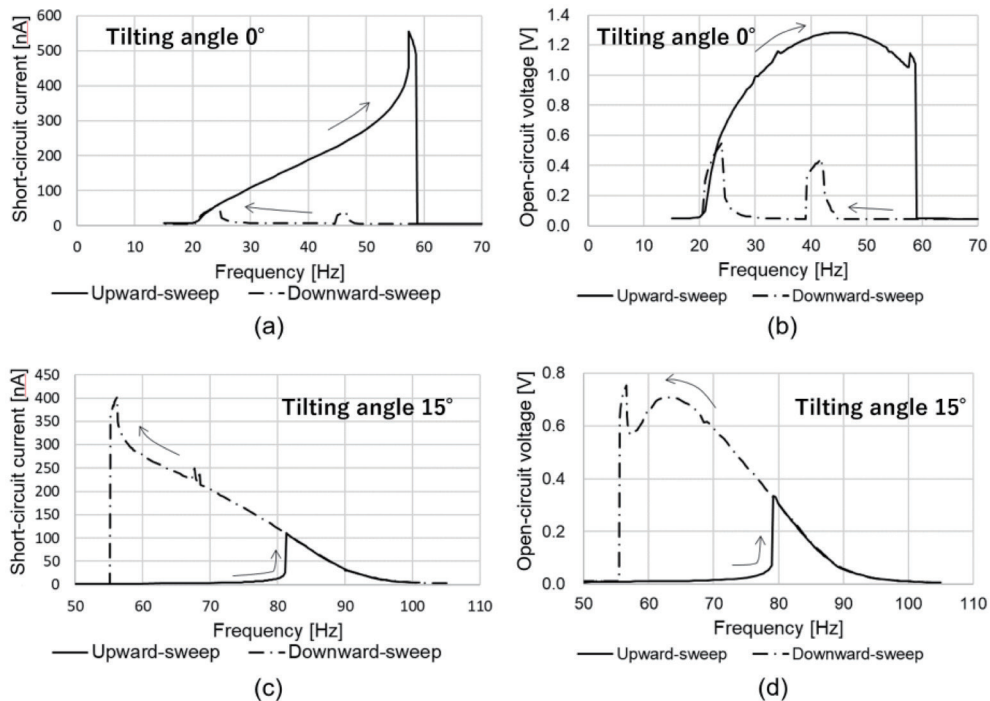


Fig. 21. Experimental results of (a) short-circuit currents and (b) open-circuit voltages at the tilting angle of 0°, and (c) short-circuit currents and (d) open-circuit voltages at the tilting angle of 15°.

an accelerometer attached to the tip of the device holder. The frequency response of the harvester is thus reconfigurable by adjusting the angle of installation. In the presented device, the frequency response range can be changed from the original 20–58 Hz for zero tilt to 55–100 Hz for 15° tilt. When the stage was set horizontal, the electrode position was out-of-phase as designed, and the output characteristics were the same as described in the previous section. When the stage was tilted 15°, on the other hand, the initial position of the electrodes was changed to in-phase, and the frequency response inclined to the low-frequency side, which agreed well with the simulation result of the in-phase electrode shown in Fig. 8(e). The output voltage and current levels measured at the zero tilt angle were greater than those at 15°, indicating that the electrodes after tilting became difficult to move owing to the electrostatic constraining force that deepened the valley of the potential curves.

Note that the data shown in Fig. 21 were obtained using the lock-in amplifier, and the current and voltage values are the contributions from a single point of frequency measurement. The output data shown in Fig. 17, on the other hand, were the RMS values contributed from all the harmonic components. As a result, the power shown in Fig. 17 became greater than that calculated from the results shown in Fig. 21.

### 5.3 In-use reconfigurable operation

Finally, we show the initial position dependence of frequency response using another device having a 11.7 g proof mass and thus, a mechanical resonant frequency of around 48 Hz. Figure 22 shows the short-circuit currents observed as the tilting angle changed. The inset photographs show the mutual initial positions of the facing protrusion electrodes. Figures 22(a) and 22(h) correspond to the out-of-phase and in-phase models, respectively, and the frequency response shows good agreement with the simulation results shown in Fig. 8. Figure 22(d) seems to show the transition state from softening to hardening natures, which is considered to be close to the half-out-of-plane model.

The in-use reconfigurability of the device in this work is beneficial for power harvesting from environmental vibrations of small magnitude and rather wide frequency range, as reported elsewhere;<sup>(12)</sup> for instance, the distinct power spreads from 20 to 100 Hz and the acceleration level is mostly 10 mG or less.

Infrastructures such as highway ducts are known to have distinctive peak vibrations but their occurrence is stochastic, depending upon the traffic condition of vehicles. This leads to frequent interruptions of power generation when the energy harvesters are designed solely for such peaks. Besides such strong vibrations, there are always faint vibrations spreading around the distinctive peaks. The devices developed in this work can cover such wide range of frequency by tailoring the frequency response by adjusting the mounting angle to the vibration sources. Recent advances in electronics have made it possible to build wireless sensor systems at a very low power; for example, the microcontroller PIC12f629 (Microchip Technology Inc.) and the timer IC TPL5010 (Texas Instruments Inc.) use only 1 nA of current during sleep and 37 nA during watchdog operation, respectively, and a sensor node made with such electronics can operate intermittently at as little as 40 nA in the sleep mode. Given the output voltage levels above the

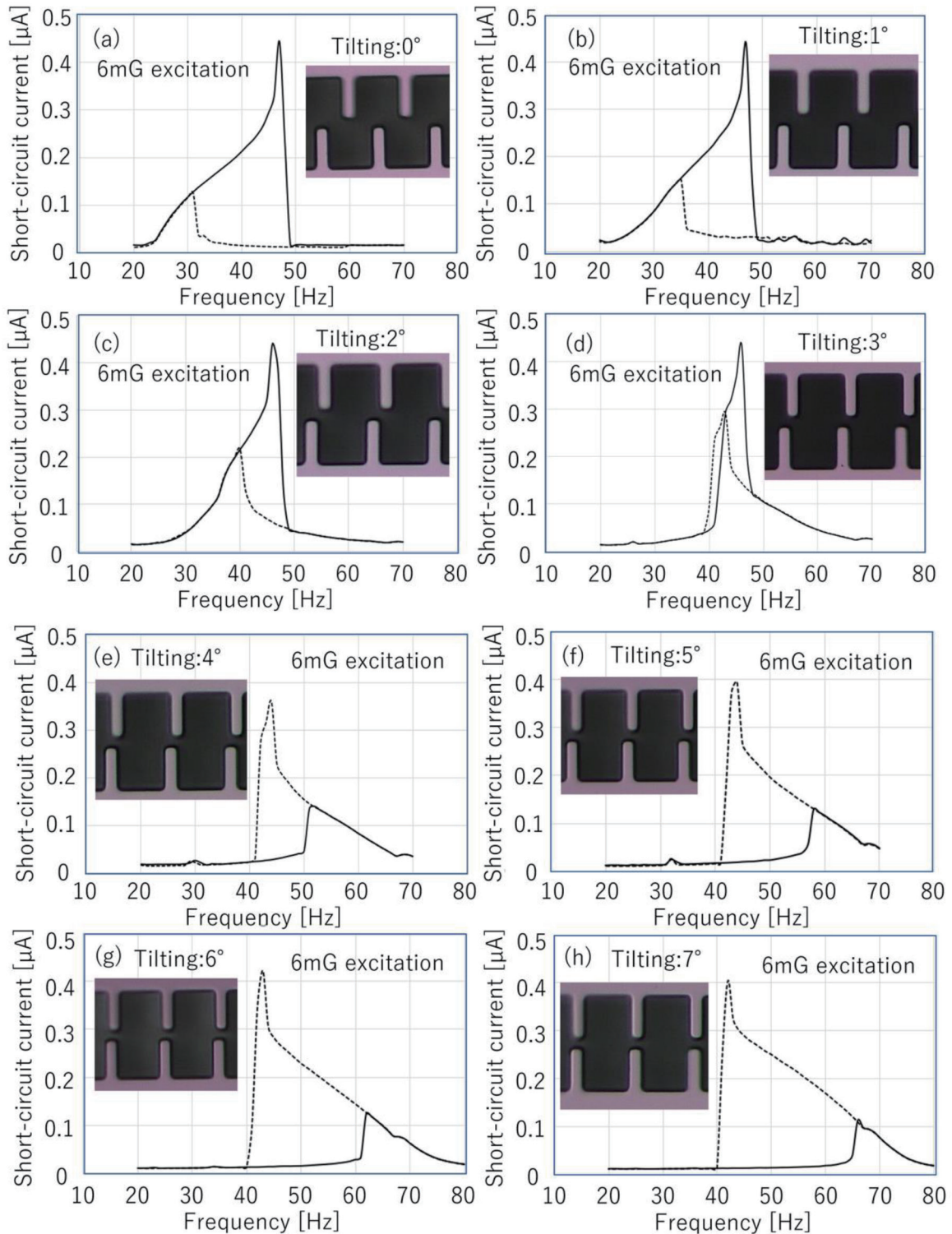


Fig. 22. (Color online) Initial mutual position dependence of frequency response observed on the short-circuit current. The inset photos were taken by changing the tilting angle. The solid lines are data for upward frequency sweeps, while the dashed lines are for downward sweeps.

typical threshold voltage of silicon diode rectifiers and the current levels of several hundred nA, the developed energy harvester is useful as a practical power source for power-autonomous sensor nodes for applications such as infrastructure monitoring.

## 6. Conclusions

In this study, we have developed a MEMS vibrational energy harvester with a wide frequency bandwidth using electret as a material for mechano-electric power conversion. The device is composed of laterally movable interdigitated electrodes having many small protrusions to cause modulation in the effective electrostatic force acting on the electrodes. The net elastic constant is effectively reduced using the electrostatic force, making the device sensitive to small vibrations. The developed harvester delivers voltages sufficiently high for most silicon diode rectifiers under acceleration as small as a few mG over a 35 Hz frequency range. The nonlinearity also results in the strong soft- and hard-spring effects, depending on the initial position of the movable electrodes with respect to the fixed ones, thereby expanding the frequency bandwidth. We have also developed an analytical model based on the equivalent linearization and derived a set of analytical equations for the effective spring constant, the results of which agree well with those of experiments.

Owing to the energy-harvesting capability in a small acceleration range in a wide frequency span, the harvester developed in this work can be used in a battery-free network sensor to continue monitoring the time-dependent degradation of social infrastructures such as bridges, highways, and railroads. A field test for such applications is under way, along with the development of commercial-use MEMS energy harvesters.

## Acknowledgments

The authors would like to thank Professor Hiroyuki Fujita with Tokyo City University, Tokyo, Japan, for his technical advice. We also acknowledge the technical support provided by Dr. Tatsuhiko Sugiyama and Dr. Yasushi Shibata. This work was supported by the New Energy and Industrial Technology Development Organization (NEDO) and JST CREST, Japan, under Grant Numbers JPMJCR15Q4 and JPMJCR19Q2.

## References

- 1 P. Glynn-Jones, S. P. Beeby, and N. M. White: *IET Sci. Meas. Technol.* **148** (2001) 68. <https://doi.org/10.1049/ip-smt:20010323>
- 2 S. P. Beeby, M. J. Tudor, and N. M. White: *Meas. Sci. Technol.* **17** (2006) R175. <https://doi.org/10.1088/0957-0233/17/12/R01>
- 3 C. Saha, T. Donnel, H. Loder, S. P. Beeby, and M. J. Tudor: *IEEE Trans. Magn.* **42** (2006) 3509. <https://doi.org/10.1109/TMAG.2006.879447>
- 4 P. D. Mitcheson, E. M. Yeatman, G. K. Rao, A. S. Holmes, and T. C. Green: *Proc. IEEE* **96** (2008) 1457. <https://doi.org/10.1109/JPROC.2008.927494>
- 5 Y. Suzuki: *IEEJ Trans. Electr. Electron. Eng.* **6** (2011) 101. <https://doi.org/10.1002/tee.20631>
- 6 M. W. Williams: *IEEE Trans. Ind. Appl.* **47** (2011) 1093. <https://doi.org/10.1109/TIA.2011.2126032>
- 7 S. Niu, Y. Liu, Y. S. Zhou, S. Wang, L. Lin, and Z. L. Wang: *IEEE Trans. Electron Devices* **62** (2015) 641. <https://doi.org/10.1109/TED.2014.2377728>

- 8 M.-G. Kang, W.-S. Jung, C.-Y. Kang, and S.-J. Yoon: *Actuators* **5** (2016) 5. <https://doi.org/10.3390/act5010005>
- 9 H. Ulsan, O. Zorlu, A. Muhtaroglu, and H. Kulah: *IEEE Trans. Ind. Electron.* **64** (2017) 5460. <https://doi.org/10.1109/TIE.2017.2677324>
- 10 H. Honma, H. Mitsuya, G. Hashiguchi, H. Fujita, and H. Toshiyoshi: *J. Micromech. Microeng.* **28** (2018) 064005. <https://doi.org/10.1088/1361-6439/aab514>
- 11 H. Toshiyoshi, S. Ju, H. Honma, C.-H. Ji, and H. Fujita: *Sci. Technol. Adv. Mater.* **20** (2019) 124. <https://doi.org/10.1080/14686996.2019.1569828>
- 12 H. Koga, H. Mitsuya, H. Honma, H. Fujita, H. Toshiyoshi, and G. Hashiguchi: *Micromachines* **8** (2017) 293. <https://doi.org/10.3390/mi8100293>
- 13 H. Liu, C. J. Tay, C. Quan, T. Kobayashi, and C. Lee: *J. Microelectromech. Syst.* **20** (2011) 1131. <https://doi.org/10.1109/JMEMS.2011.2162488>
- 14 X. Tang and L. Zuo: *J. Sound Vib.* **330** (2011) 5199. <https://doi.org/10.1016/j.jsv.2011.05.019>
- 15 T. Masaki, N. Yoshitake, S. Kamiyama, M. Nabeto, T. Seki, M. Oba, and D. Uchida: *J. Phys. Conf. Ser.* **557** (2014) 012074. <https://doi.org/10.1088/1742-6596/557/1/012074>
- 16 S. D. Nguyen and E. Halvorsen: *J. Microelectromech. Syst.* **20** (2011) 1225. <https://doi.org/10.1109/JMEMS.2011.2170824>
- 17 Q. C. Tang and X. Li: *The 17th Int. Conf. Solid-State Sensors, Actuators and Microsystems (Transducers & Eurosensors XXVII)* (2013) 697. <https://doi.org/10.1109/Transducers.2013.6626862>
- 18 C. Trigona, F. Giusa, F. Maiorca, A. Noto, B. Ando, and S. Baglio: *IEEE Sensors Applications Symp. (SAS)* (2014) 166. <https://doi.org/10.1109/SAS.2014.6798939>
- 19 B. Ando, S. Baglio, G. L'Episcopo, and C. Tri: *J. Microelectromech. Syst.* **21** (2012) 779 <https://doi.org/10.1109/JMEMS.2012.2192912>
- 20 B. Ando, S. Baglio, A. R. Bulsara, V. Marletta, and A. Pistorio: *IEEE Trans. Instrum. Meas.* **66** (2017) 1067. <https://doi.org/10.1016/j.jsv.2009.11.034>
- 21 F. Cottone, L. Gammaïtoni, H. Vocca, M. Ferrari, and V. Ferrari: *Smart Mater. Struct.* **21** (2012) 035021 <https://doi.org/10.1088/0964-1726/21/3/035021>
- 22 G. Despesse, J. J. Chaillout, T. Jager, F. Cardot, and A. Hoogerwerf: *Transducers* **2007** (2007) 895. <https://doi.org/10.1109/SENSOR.2007.4300275>
- 23 K. Murotani and Y. Suzuki: *J. Micromech. Microeng.* **28** (2018) 104001. <https://doi.org/10.1088/1361-6439/aac8cc>
- 24 T. Sugiyama, M. Aoyama, Y. Shibata, M. Suzuki, T. Konno, M. Ataka, H. Fujita, and G. Hashiguchi: *Appl. Phys. Express* **4** (2011) 114103. <https://doi.org/10.1143/APEX.4.114103>
- 25 Y. Shibata, T. Sugiyama, H. Mimura, and G. Hashiguchi: *J. Microelectromech. Syst.* **24** (2015) 1052. <https://doi.org/10.1109/JMEMS.2014.2379959>
- 26 G. Hashiguchi, D. Nakasone, T. Sugiyama, M. Ataka, and H. Toshiyoshi: *AIP Adv.* **6** (2016) 035004. <https://doi.org/10.1063/1.4943528>
- 27 G. Hashiguchi: *IEICE Electron. Express* **11** (2014) 1. <https://doi.org/10.1587/elex.11.20142007>
- 28 H. Honma, Y. Tohyama, H. Mitsuya, G. Hashiguchi, H. Fujita, and H. Toshiyoshi: *J. Micromech. Microeng.* **29** (2019) 084002. <https://doi.org/10.1088/1361-6439/ab2371>.

## About the Authors

**Gen Hashiguchi** received his M.S. degree in electrical engineering from Chuo University, Tokyo, Japan, in 1988, and his Ph.D. degree in electrical engineering from The University of Tokyo, Tokyo, Japan, in 1996. From 1988 to 1998, he was with Nippon Steel Corporation, where he was involved in the development of microdevices, including thermal sensors, field emitters, and amorphous silicon imaging sensors. In 1999, he became a professor of mechanical engineering at Kagawa University, Kagawa, Japan, and in 2007, he joined the Research Institute of Electronics, Shizuoka University. His current research interests are MEMS with an emphasis on electret devices. ([Hashiguchi.gen@shizuoka.ac.jp](mailto:Hashiguchi.gen@shizuoka.ac.jp))

**Hiroshi Toshiyoshi** received his M.E. and Ph.D. degrees in electrical engineering from The University of Tokyo, Tokyo, Japan, in 1993 and 1996, respectively. He joined the Institute of Industrial Science (IIS), The University of Tokyo in 1996 as a lecturer. From 1999 to 2001, he was a Visiting Assistant Professor at the University of California, Los Angeles, CA, USA. In 2002, he became an associate professor with the IIS, The University of Tokyo. From 2005 to 2008, he was the project leader of the Optomechatronics Project at Kanagawa Academy of Science and Technology, Kawasaki, Japan. Since 2009, he has been a professor with the IIS, The University of Tokyo. His research interests include optical and RF-MEMS (microelectromechanical systems). ([hiro@iis.u-tokyo.ac.jp](mailto:hiro@iis.u-tokyo.ac.jp))